Sensitivity and specificity of CEST and NOE MRI in injured spinal cord in monkeys

Feng Wang [a,b], Zhongliang Zu [a,b], Tung-Lin Wu [a,c], Xinqiang Yan [a,b], Ming Lu [a,b], Pai-Feng Yang [a,b], Nellie E. Byun [a,b], Jamie L. Reed [a,b], John C. Gore [a,b,c,1], Li Min Chen [a,b,1,*]

[a] *Vanderbilt University Institute of Imaging Science, Vanderbilt University Medical Center, USA*
[b] *Department of Radiology and Radiological Sciences, Vanderbilt University Medical Center, TN, USA*
[c] *Department of Biomedical Engineering, Vanderbilt University, TN, USA*

ARTICLE INFO

ABSTRACT

Purpose: The sensitivity and accuracy of chemical exchange saturation transfer (CEST) and nuclear Overhauser enhancement (NOE) effects for assessing injury-associated changes in cervical spinal cords were evaluated in squirrel monkeys. Multiple interacting pools of protons, including one identified by an NOE at -1.6 ppm relative to water (NOE(-1.6)), were derived and quantified from fitting proton Z-spectra. The effects of down-sampled data acquisitions and corrections for non-specific factors including T_1, semi-solid magnetization transfer, and direct saturation of free water (DS), were investigated. The overall goal is to develop a protocol for rapid data acquisition for assessing the molecular signatures of the injured spinal cord and its surrounding regions.
Methods: MRI scans were recorded of anesthetized squirrel monkeys at 9.4 T, before and after a unilateral dorsal column sectioning of the cervical spinal cord. Z-spectral images at 51 different RF offsets were acquired. The amplitudes of CEST and NOE effects from multiple proton pools were quantified using a six-pool Lorenzian fitting of each Z-spectrum (MTR$_{mfit}$). In addition, down-sampled data using reduced selections of RF offsets were analyzed and compared. An apparent exchange-dependent relaxation (AREX$_{mfit}$) method was also used to correct for non-specific factors in quantifying regional spectra around lesion sites.
Results: The parametric maps from multi-pool fitting using the complete sampling data (P51e) detected unilateral changes at and around the injury. The maps derived from selected twofold down-sampled data with appropriate interpolation (P26sI51) revealed quite similar spatial distributions of different pools as those obtained using P51e at each resonance shift. Across 10 subjects, both data acquisition schemes detected significant decreases in NOE (-3.5) and NOE(-1.6) and increases in DS(0.0) and CEST(3.5) at the lesion site relative to measures of the normal tissues before injury. AREX$_{mfit}$ of cysts and other abnormal tissues at and around the lesion site also exhibited significant changes, especially at 3.5, -1.6 and -3.5 ppm RF offsets.
Conclusion: These results confirm that a reduced set of RF offsets and down sampling are adequate for CEST imaging of injured spinal cord and allow shorter imaging times and/or permit additional signal averaging. AREX$_{mfit}$ correction improved the accuracy of CEST and NOE measures. The results provide a rapid (~13 mins), sensitive, and accurate protocol for deriving multiple NOE and CEST effects simultaneously in spinal cord imaging at high field.

1. Introduction

The normal functions of the spinal cord can be disrupted by traumatic spinal cord injuries (SCI), which induce sensory, motor, and autonomic functional deficits. The initial injury may cause cell death and lead to cascades of destructive secondary injury processes including inflammation and edema in the acute phase, and demyelination and formation of cysts in the subacute and chronic phases following injury (Guest et al., 2005; Totoiu and Keirstead, 2005; Thuret et al., 2006). These different phases are characterized by distinct pathological

Fig. 1. Characteristic features of Z-spectra of tissues in the injured spinal cord of squirrel monkey. (A) Anatomical images with magnetization transfer contrast showing the unilateral dorsal column lesion in the cervical spinal cord. Arrows indicate the lesion site. The dotted lines in the left and middle panels indicate the coronal orientation, and the dashed lines in the middle and right panels indicate the midline of spinal cord. V: ventral; D: dorsal; r: rostral; c: caudal; L: lesion side; N: non-lesion side; Les, lesion; cDL: caudal to the lesion; rDL, rostral to the lesion; sDL, lateral side to the lesion; Ctrl, non-lesion control side; CSF: cerebrospinal fluid. (B) 6-pool Lorentzian band fitting of normal and abnormal tissues on in the control and lesion regions of spinal cord, respectively. Peaks were assigned at RF offset frequencies of −3.5 (I), −1.6 (II), 0 (III), 1.0 (IV), 2.0 (V), and 3.55 (VI) ppm. The amplitude and width of the peaks were allowed to vary for achieving the best fit. The bottom half of the figure shows the residuals between the sum of the fitted peaks and the original data.

changes which may be potential targets for interventions. These interactive and dynamic processes are not well understood, partially due to the lack of suitable monitoring tools. Non-invasive, multi-parametric, magnetic resonance imaging (mpMRI) methods allow detection and monitoring of the injury itself as well as injury-associated structural, functional and molecular changes over time (Stroman et al., 2014; Wheeler-Kingshott et al., 2014; Chen et al., 2015; Wang et al., 2015, 2016b, 2018b, 2019; Yang et al., 2015; Wu et al., 2020). In previous studies, we have studied injured spinal cords of non-human primates (NHPs) using a mpMRI protocol, including chemical exchange saturation transfer (CEST) (Wang et al., 2015, 2018b), relayed nuclear Overhauser enhancement (NOE) (Wang et al., 2015, 2018b), diffusion tensor imaging (DTI) (Wang et al., 2015; Mishra et al., 2020), quantitative magnetization transfer (qMT) (Wang et al., 2016b, 2019), and functional MRI (fMRI) (Chen et al., 2015; Yang et al., 2015). These advanced quantitative MRI methods have allowed us to delineate the damage to injured spinal cord at the compartment level and across several spinal segments around the injury site for up to 6 months post injury (Chen et al., 2015; Wang et al., 2015, 2016b, 2018b, 2019; Wu et al., 2019).

Among advanced MRI measures, CEST and NOE effects derived from Z-spectra can in principle be used to quantify changes in metabolites,

mobile proteins and membrane lipids associated with the secondary injury and inflammation after SCI, and during the repair and recovery processes. Changes in CEST and NOE effects have been observed in neurological disorders (Zhang et al., 2016), renal disease (Wang et al., 2016a, 2018b), cancer (Zhang et al., 2017a, 2017b), and SCI (Wang et al., 2015, 2018b). A common approach assumes protons reside in multiple pools (free water, chemically exchanging moieties, and both relatively immobile and mobile macromolecules) (Wang et al., 2016a, 2018a). The CEST and NOE effects can be separated from other types of magnetization transfer and direct water saturation (DS) by fitting Z-spectra to a sum of selected resonances (Wang et al., 2016a, 2018b). We have previously shown that 5-pool fitting provides CEST and NOE measures for detecting injury-associated pathological changes in the spinal cords of non-human primates (Wang et al., 2018b). This approach resulted in quantification of CEST and NOE signals that are important for practical applications, but the acquisition of a densely sampled high resolution Z-spectra takes a long time and the obtained measures are still influenced by T_1 effects (Zhang et al., 2017a, 2017b).

The current study aims to develop a rapid CEST and NOE imaging protocol that allows detection and monitoring of injury-associated molecular composition changes with high sensitivity and specificity in

multiple spinal regions at and around an injury site. We focused on three aspects. First, besides the CEST pool around 1.0 ppm RF offset which is evident in some injured spinal cords (Wang et al., 2015, 2018b), we included an additional NOE(-1.6) pool in the fittings because it is known to be altered in some pathologies such as stroke and cancer (Zhang et al., 2016, 2017a, 2017b), and evaluated the sensitivity and specificity of 6 pools to injury-associated regional changes. Second, to improve the specificity of measures and to reduce the contributions from non-specific factors such as variations in T$_1$, semi-solid magnetization transfer (MT), and direct water saturation (DS), we applied an inverse subtraction analysis and derived parameters, termed apparent exchange-dependent relaxation (AREX$_{mfit}$), to report the results (Zaiss et al., 2014; Zhang et al., 2017a, 2017b). Third, we evaluated the influence on the results of 6-pool fitting from using a reduced set of Z-spectral images obtained by down sampling the number of RF offsets in Z-spectral data, and compared the sensitivity and specificity of the measurements to those derived from complete data with 51 RF offsets. We used a well-established NHP SCI model that closely resembles human spinal cord injuries (Kaas et al., 2008), which increases the clinical relevance of the MRI data acquisitions and measures evaluated. Here we show that a robust and sensitive CEST and NOE protocol is achievable in a reasonable time window.

2. Material and methods

2.1. Spinal cord injury model - unilateral dorsal column lesion

The dorsal portion of the lower cervical spinal cord at C4-C6 level was exposed under surgical level of anesthesia and aseptic conditions. The dorsal column pathway (tract) was transected on the side related to preferred hand usage with a pair of fine surgical scissors at the C5 level. Each lesion was 2 mm deep and ran from the midline to the spinal nerve entering zone (~2 mm in width). Dura was replaced with a small piece of gelfilm, and the wound was enclosed. Standard post-surgery care including administration of analgesics were performed per standard animal care protocol. The details of the surgical procedures can be found in previous publications (Qi et al., 2011, 2016; Chen et al., 2012).

2.2. Animal preparation

Ten male adult squirrel monkeys (*Saimiri sciureus*) were studied. These monkeys were scanned before and after SCI, at the time point when the behavioral deficits in hand use were severe after injury (Qi et al., 2016; Wang et al., 2018b). Throughout each MR imaging session, each monkey was anesthetized (isoflurane 0.5–1.2%) and mechanically ventilated (40 respiration cycles/min), with head and body stabilized in an MR-compatible frame. Vital signs such as core body temperature, SpO$_2$, end-tidal CO$_2$, respiration rate, and heart rate, were monitored and maintained at stable levels. All procedures followed NIH guidelines on the care and use of laboratory animals and were approved by IACUC (Institutional Animal Care and Use Committee) of Vanderbilt University.

2.3. In vivo MRI

All MRI data were acquired on a Varian DirectDrive^{TM} horizontal 9.4 T scanner using a saddle-shaped transmit-receive surface coil positioned around the cervical spine region. The image field of view was centered at the level where the lesion was targeted. After acquiring high resolution structural images with magnetization transfer contrast (MTC) to guide the placements of image slices (Fig. 1A), Z-spectral images were acquired using a 5 s continuous wave (CW) saturation of amplitude 1.0 μT at different RF offsets from the water resonance, followed by a spin-echo echo-planar-imaging acquisition (TR/TE = 7500/18 ms, 2 shots, resolution = 0.5x0.5 mm^2, slice thickness = 1 mm). We selected low irradiation power 1.0 μT to support multi-peak fitting based on previous studies (Desmond et al., 2014; Zhang et al., 2017a, 2017b). Images with

each of 51 different RF offsets equally spaced from −5 ppm to 5 ppm relative to water were acquired. Additional reference images were acquired with RF offset 250 ppm. The effective longitudinal relaxation rate R$_{1obs}$ was obtained based on images acquired with two flip angles (Smith et al., 2008).

2.4. Data Analyses

All MRI data were analyzed using MATLAB (The Mathworks, Natick, MA, US). High-resolution MTC weighted images were referenced for manual selection of ROIs (regions of interests) for quantification (Fig. 1A), including normal gray matter (GM) and white matter (WM) on the control side (Ctrl), cyst on the lesion side (identified by its hyper-intensity in MTC images), abnormal tissues at the level of lesion (Les), and abnormal tissues caudal (cDL), rostral (rDL) and lateral to (sDL) the lesion (Fig. 1A). Only regions with homogeneous B$_0$ and B$_1$ ($|\Delta B_0| <$ 100 Hz, and $|\Delta B_{1ratio}| < 0.05$) were selected and included in the ROI analysis (Sup. Fig. S1). To minimize partial volume effects, small ROIs were selected and voxels residing along the SC – CSF border were excluded. A linear baseline correction was applied to the Z-spectra based on the reference scans at 250 ppm RF offset, and B$_0$-corrections were based on using a water saturation shift reference spectrum (WASSR) (Kim et al., 2009). The details were described in our previous work (Wang et al., 2018b).

Z-spectra were obtained by normalizing the signal at each RF offset (S) to the signal obtained with offset 250 ppm (S$_o$; Z = S/S$_o$). The peak amplitudes of CEST effects at three RF offsets around 1.0, 2.0 and 3.55 ppm, DS at 0.0 ppm RF offset; and NOE effects at two RF offsets around −1.6 and −3.5 ppm, were quantified using a 6-pool Lorentzian fitting of each Z-spectrum (Fig. 1B and Sup. Table S1). The comparisons of 4-pool (Desmond et al., 2014), 5-pool (Wang et al., 2018b) and 6-pool fitting of normal and abnormal tissues in injured spinal cord are shown in supporting Fig. S2, and the fitting quality is the best from 6-pool fitting as shown by its lowest root-mean-square deviation (RMSD).

A label signal (S$_{lab}$) for each pool denotes the fitted value of its Z-spectrum at a specific offset Δω, whereas a reference signal is obtained by adding all the other fitted Lorentzians except the contribution of that pool (Zhang et al., 2017a, 2017b). The difference between the label and reference signal values, normalized to S$_o$, is MTR$_{mfit}$.

$$MTR_{mfit}(\Delta\omega) = \frac{S_{ref}(\Delta\omega) - S_{lab}(\Delta\omega)}{S_0}$$

The derived values were named as NOE(-3.5), NOE(-1.6), DS(0.0), CEST(1.0), CEST(2.0) and CEST(3.5), for MTR$_{mfit}$ obtained at RF offsets −3.5 (pool I), −1.6 (pool II), 0.0 (pool III), 1.0 (pool IV), 2.0 (pool V), and 3.55 (pool VI) ppm respectively.

The fitting results based on all the equally spaced sampling data from 51 RF offsets (P51e) were quantified first and used as standards for comparison. The down-sampled data with different reduced selections of RF offsets were analyzed using the same approach. We considered down-sampled data using equally spaced 26 RF offsets (P26e) with intervals at 0.4 ppm, and equally spaced 17 RF offsets (P17e) with intervals at 0.6 ppm. Based on the common peak widths measured for different pools of normal tissue in spinal cord, we also selected 26 RF offsets (P26s) and selected 22 RF offsets (P22s) with different intervals in the domain of each pool. The fitting results of the above down-sampled data were obtained and compared to those from P51e. The effect of spline interpolation was also investigated. The down-sampled data P17e, P26e, and P26s with further spline interpolation to 51 RF offsets were named as P17eI51, P26eI51, P26sI51, respectively. The correlations between results derived from P26sI51 and P51e for each specific CEST and NOE effect were evaluated using linear regression.

AREX$_{mfit}$ values were derived by subtracting the inverses of the reference and label signals with T$_{1obs}$ (=1/R$_{1obs}$) normalization (Zhang et al., 2017a, 2017b).
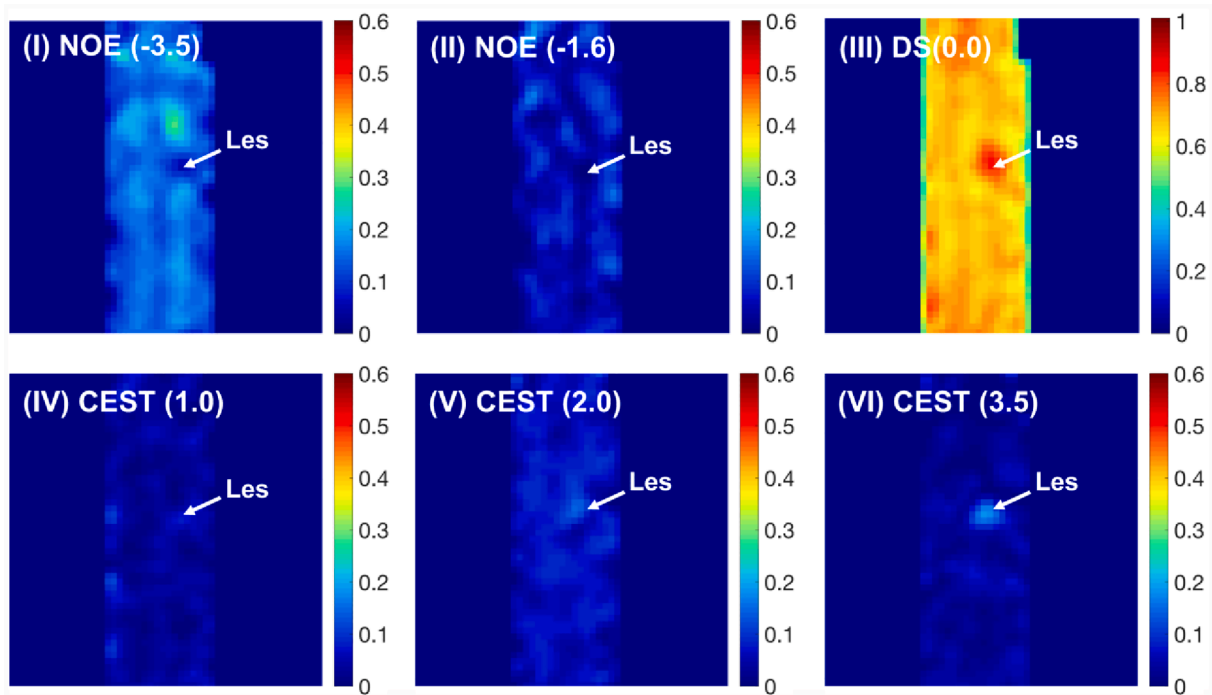
Fig. 2. The maps of peak amplitudes at different RF offsets from MTR$_{mfit}$, zoomed on the regions with homogeneous B$_0$ and B$_1$. Peaks were assigned at RF offset frequencies of −3.5 (I), −1.6 (II), 0 (III), 1.0 (IV), 2.0 (V), and 3.55 (VI) ppm.
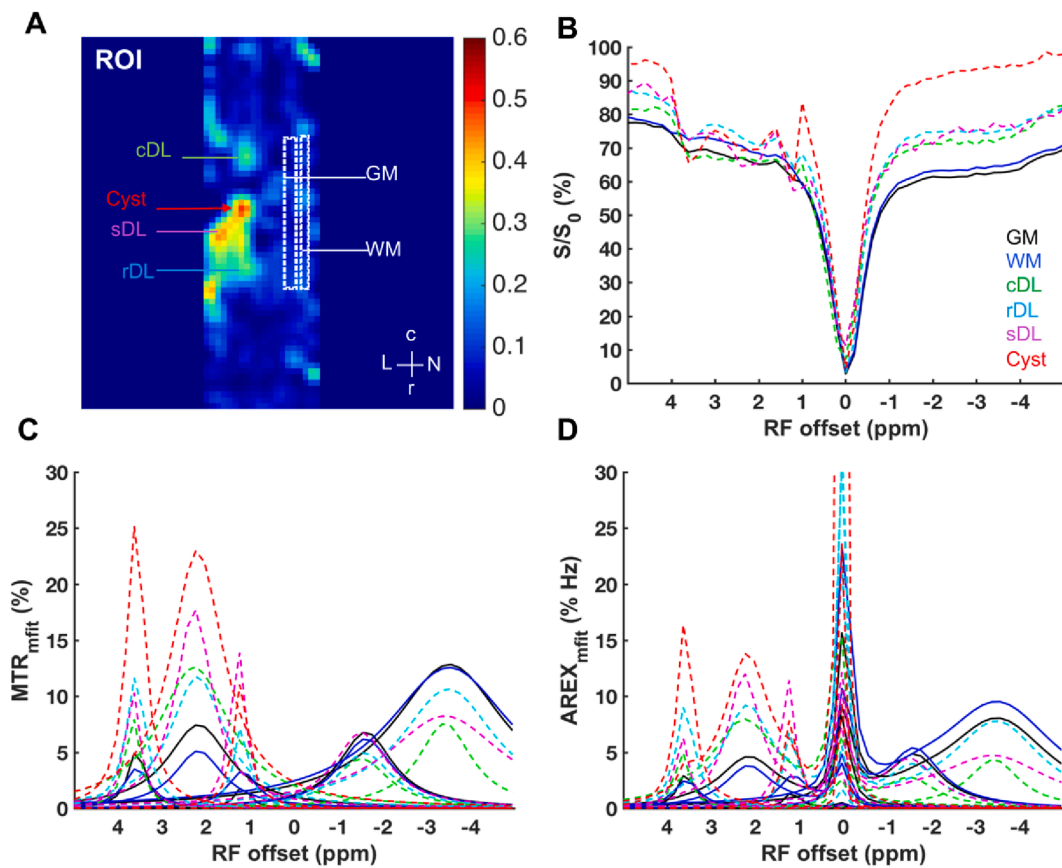

Fig. 3. Representative regional AREX$_{mfit}$ results. (A) Six regions of interest in the injured spinal cord, shown in the CEST(2.0 ppm) map. GM: gray matter; WM: white matter; rDL, cDL, and sDL: rostral, caudal, and lateral tissues next to lesion side; Cyst: formed at lesion site and confirmed by histology sections. r: rostral; c: caudal; L: lesion side; N: non-lesion side. (B) Regional Z-spectra. (C) Regional multi-pool MTR$_{mfit}$ without R$_1$ correction. (D) Regional multi-pool AREX$_{mfit}$ results.

$$AREX_{mfit}(\Delta\omega) = \left(\frac{S_0}{S_{lab}(\Delta\omega)} - \frac{S_0}{S_{ref}(\Delta\omega)}\right) R_{1obs}(1 + f_c)$$

where f_c is the semisolid MT pool size ratio (PSR) from quantitative magnetization transfer imaging (Wang et al., 2016b, 2019). The derived peak amplitudes were named as $NOE_c(-3.5)$, $NOE_c(-1.6)$, $DS_c(0.0)$, $CEST_c(1.0)$, $CEST_c(2.0)$, and $CEST_c(3.5)$, for $AREX_{mfit}$ obtained at RF offsets -3.5 (pool I), -1.6 (pool II), 0.0 (pool III), 1.0 (pool IV), 2.0 (pool V), and 3.55 (pool VI) ppm, respectively. $AREX_{mfit}$ is independent of non-specific tissue parameters T_1, DS, and semi-solid MT effects, and it only depends on solute concentration, solute-water exchange rate, solute transverse relaxation and irradiation power (Zhang et al., 2017a, 2017b).

The differences in regional pool amplitudes were evaluated using Student's t-tests, and FDR (false discovery rate) corrected $p < 0.05$ was considered as significant. Receiver operating characteristic (ROC) curves (Hajian-Tilaki 2013) were also constructed to compare the true positive rates (sensitivity) and false positive rates (1-specificity) of MRI measures.

3. Results

3.1. Characteristic features of Z-spectra of tissues in the injured spinal cord

The lesion created by a unilateral dorsal column section can be identified after injury (Fig. 1A). Fig. 1B shows representative fitting results for normal and abnormal tissues obtained with complete sampling data (P51e), delineating the peak amplitude and width of each CEST and NOE resonance in the cord after injury. The lesion showed increased amplitudes for CEST and DS pools and decreased amplitudes for NOE pools compared to the control (Fig. 1B and Sup. Table S2). NOE(-1.6) and NOE(-3.5) showed broader peak widths (>2 ppm) than other pools in general (Fig. 1B and Sup. Table S2). While CEST(2.0), CEST(1.0) and DS(0.0) showed moderate peak widths (0.7–1.4 ppm), CEST(3.5) showed the narrowest peak width (~0.6 ppm) among all six pools for either normal or abnormal tissues (Fig. 1 and Sup. Table S2). These common features for the six pools were used to guide the selection of sparse intervals for broad peaks NOE(-1.6) and NOE(-3.5); relatively sparse intervals for the DS(0.0), CEST(1.0), and CEST(2.0) with moderate widths; but dense intervals for the narrow CEST(3.5) in data downsampling.

3.2. CEST and NOE maps of MTR_mfit reveal spatial changes in the injured spinal cord

The respective spatial changes of peak amplitudes from the representative injured subject are shown in the maps in Fig. 2. All the CEST and NOE maps from multi-pool fitting of complete data (P51e) detected unilateral changes at the site of the dorsal column lesion, especially in the dorsal pathway and dorsal horns on the side of injury (Fig. 2). The lesion showed significant decreases in NOE(-3.5) and NOE(-1.6) and increases in DS(0.0), CEST(1.0), CEST(2.0), and CEST(3.5) (Fig. 2). The CEST and NOE effects of tissues around the lesion site could also change when the injury was severe (Sup. Fig. S3). Individual subject differences in severity of the injury were indicated by variations in peak amplitudes, areas, and locations of the abnormal regions (Sup. Fig. S3).

3.3. Effects of AREX_mfit correction on regional CEST and NOE measurements

$AREX_{mfit}$ can reduce contributions from several non-specific factors, including T_1 and semi-solid MT effects. A subject with severe injury was selected to show regional changes at and around the lesion site (Fig. 3). Regional T_{1obs} was 1.925, 1.585, 1.976, 1.600, 2.001, and 2.366 sec for GM, WM, rDL, cDL, sDL, and Cyst, respectively. Regional f_c was 0.086,
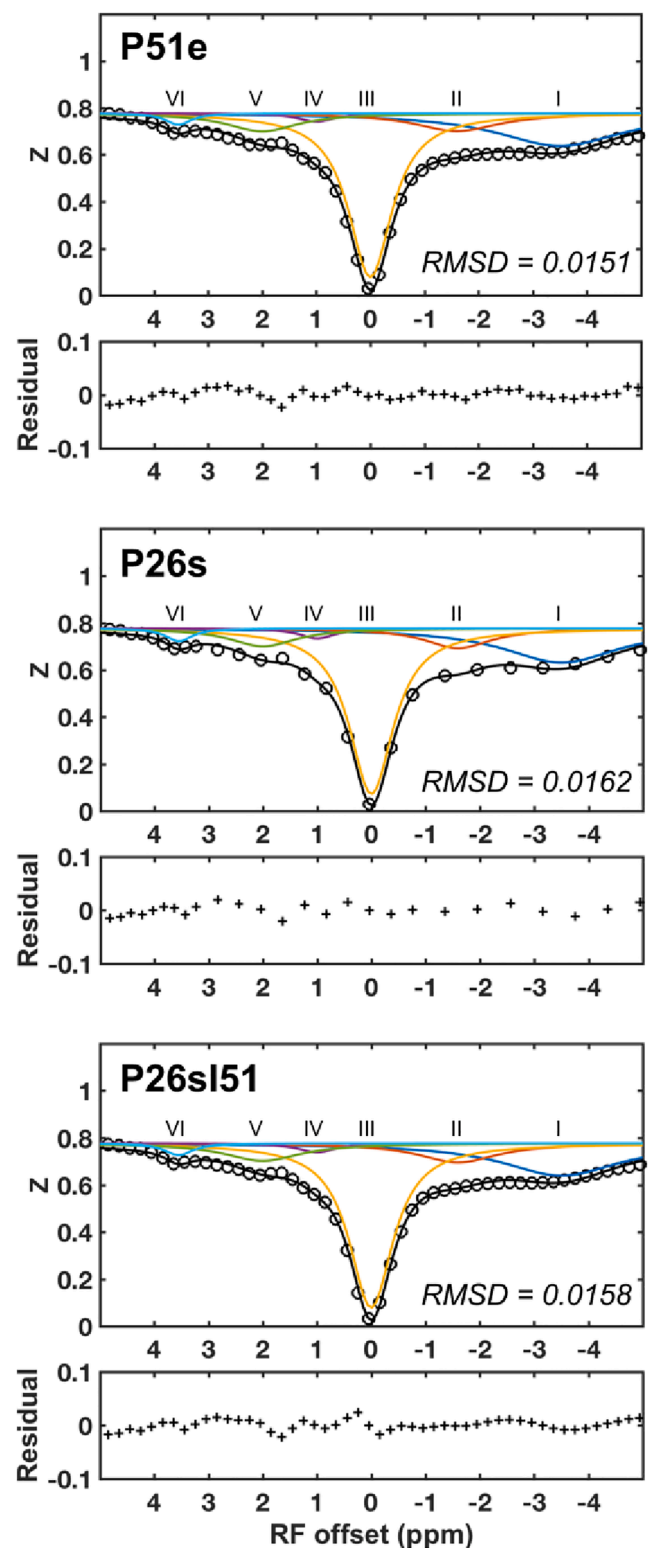

**Fig. 4.** Impact of down sampling and interpolation on the multi-pool fitting results. P51e: equally spaced CEST data with 51 RF offsets respectively (0.2 ppm intervals); P26s: CEST data with selected 26 RF offsets (different intervals for different RF offset ranges). P26sI51: CEST data with 51 RF offsets from spline interpolation of down-sampled P26s. RMSD: root-mean-square deviation of model fitting.
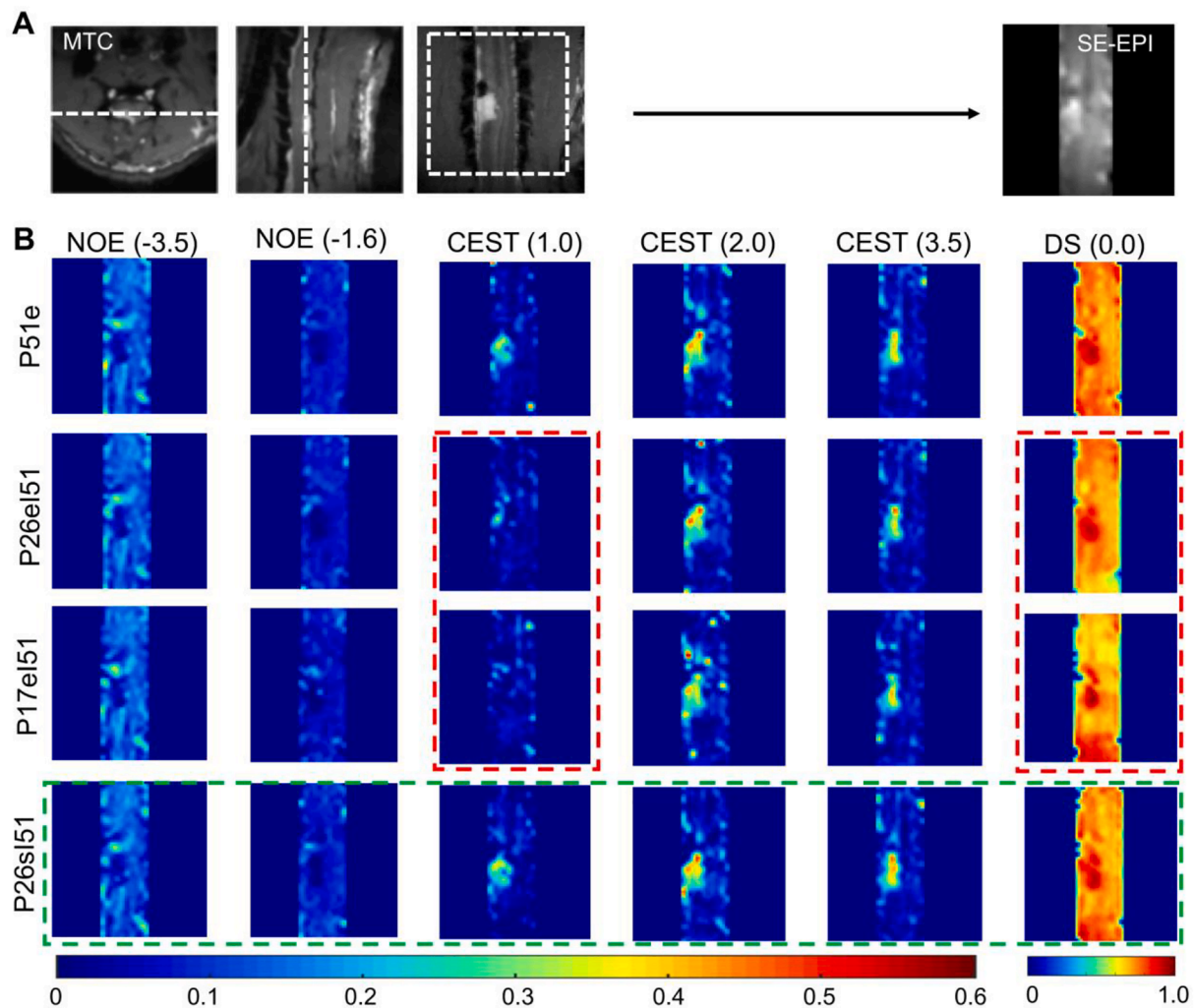
Fig. 5. Peak amplitudes of MTR$_{mfit}$ using selected down-sampled CEST data. (A) Coronal slice across dorsal column was selected for CEST imaging, indicated by the white dashed lines on transverse and sagittal images and white box on the coronal image. (B) CEST, DS, and NOE maps from selected down-sampled CEST data. P51e, P26eI51, and P17eI51: equally spaced CEST data with 51, 26, and 17 RF offsets respectively (0.2, 0.4, and 0.6 ppm intervals, respectively); P26sI51: CEST data with selected 26 RF offsets (different interval for different RF offset range). Spline interpolation (0.2 ppm interval) was applied to the above down-sampled data before model fitting. Red dashed box shows that CEST(1.0) was more affected by down-sampling. Green dashed box points out similar spatial distributions of P26sI51 compared to P51e at each RF offset. Data is from one subject 10 weeks after severe injury. (For interpretation of the references to colour in this figure legend, the reader is referred to the web version of this article.)

0.121, 0.079, 0.080, 0.078, and 0.029 for GM, WM, rDL, cDL, sDL, and Cyst, respectively. Representative AREX$_{mfit}$ values in the cyst regions showed significant increases at 3.5 and 2.0 ppm and decreases at −1.6 and −3.5 ppm (Fig. 3) compared to the corresponding measures of GM and WM on the non-lesion side 10 weeks after injury. In addition, abnormal tissues in the regions next to the lesion site (cDL, rDL and sDL regions in Fig. 3) also exhibited significant changes in AREX$_{mfit}$. The correction of background signals and T$_1$ effects on cyst regions was greater than for other abnormal tissues around the lesion as cysts have higher T$_1$ values and lower semi-solid MT effects than other abnormal regions.

3.4. Impact of data down sampling and interpolation on multi-pool fitting

The influences of the number and spacings of RF offsets on multi-pool fitting results for the averaged Z-spectrum of normal tissues were evaluated (Fig. 4, Sup. Fig. S4, and Sup. Table S3). Because the peak widths of NOE and other CEST pools were about triple and double of CEST(3.5) respectively, we obtained down-sampled data P26s (Fig. 4) by selecting RF offsets using relatively sparse intervals (0.6 ppm) for

NOE(-1.6) and NOE(-3.5) domains; applying relatively dense intervals (0.4 ppm) for DS(0.0), CEST(1.0), and CEST(2.0); but dense intervals (0.2 ppm) for CEST(3.5). The results from several other down-sampling schemes tested are shown in supporting Fig. S4 for comparison. The RMSD values from the fitting of fully sampled data P51e and down-sampled data P26e, P17e, P22s, P26s, and P26sI51 were 0.0151, 0.0158, 0.0183, 0.0185, 0.0162, and 0.0158, respectively. The twofold reduction in number of RF offsets (P26e and P26s) yielded comparable fitting quality with P51e based on the RMSD (Fig. 4 and Sup. Fig. S4). The RMSD values of the fitting from further down-sampled data P17e and P22s were much larger, and the peak amplitudes from these down-sampled data showed much larger differences from P51e compared to those from P26s and P26e, especially for CEST(1.0) (Fig. 4, Sup. Fig. S4, and Sup. Table S3). Appropriate interpolation (P26sI51) improved the accuracy of the modeling results, with reduced RMSD and peak amplitudes closer to those from P51e compared to down-sampled data without interpolation P26s (Fig. 4 and Sup. Table S3). Our results showed that the selection of down-sampled data based on common peak features of tissues in spinal cord (P26s) provided fitting results closest to those of P51e.
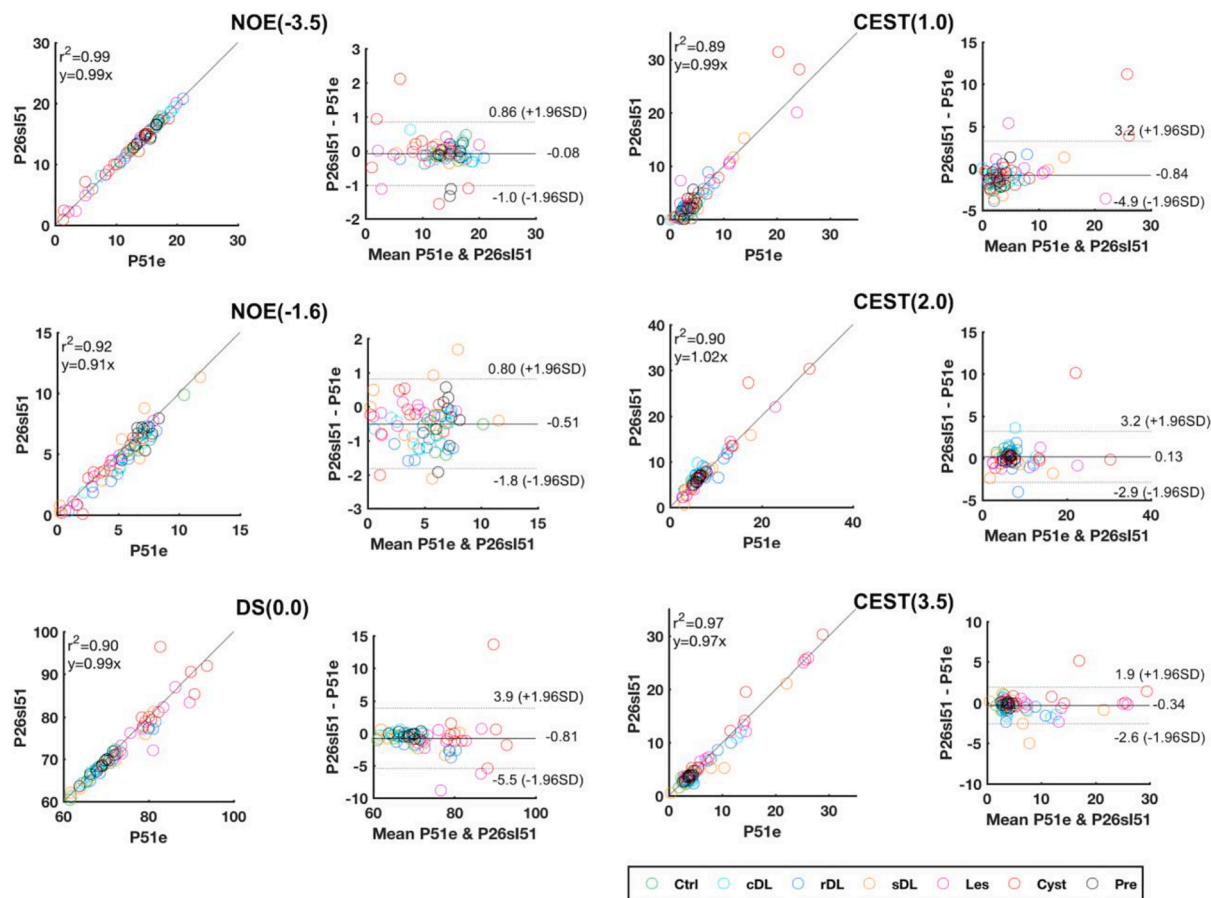
Fig. 6. The comparison of regional MTR$_{mfit}$ measures between P51e and P26sI51. In the Bland-Altman plots, solid line represents the mean difference between measures from the two approaches, whereas the dotted lines are 95% limits of agreement. Results from 7 ROIs of 10 subjects were included for comparison.

3.5. Comparison of MTR$_{mfit}$ maps derived from complete and down-sampled spectra

The CEST and NOE maps from complete and down-sampled data are compared in Fig. 5. Only the maps derived from P26sI51 showed quite similar spatial distributions to those obtained using P51e at different RF offset (indicated by green box in Fig. 5), including CEST(1.0). Conventional MTR$_{asym}$ maps and 3-point CEST$_{3p}$(3.5) and NOE$_{3p}$(-3.5) measures from down-sampled data were also compared (Sup. Fig. S5). Equally spaced down-sampling P26eI51 and P17eI51 highly affected 3-point CEST estimates around 3.5 ppm RF offset, while selected down-sampling P26sI51 showed maps quite similar to P51e for all the conventional measures (Sup. Fig. S5). The map of CEST(1.0) was more affected by down-sampling (see red box in Fig. 5) when more sparse RF intervals were applied.

3.6. Group comparison of peak amplitudes of MTR$_{mfit}$

Because P26sI51 showed comparable fitting results as P51e, further comparisons were made between them. The peak amplitudes from P26sI51 of 10 subjects were highly correlated to those using P51e (Fig. 6) at each RF offset. NOE(-3.5) and CEST(3.5) from P26sI51 showed higher correlation (r at 0.99 and 0.98 respectively) than other pools with respect to results from P51e. The peak amplitudes at RF offsets further away from water showed higher correlations between P26sI51 and P51e, indicating that they were less affected by data down-sampling.

The percent peak amplitudes of MTR$_{mfit}$ at different RF offsets showed quite similar trends across subjects using both P26sI51 and P51e (Fig. 7). CEST increased while NOE decreased at the lesion site/cyst, and

NOE(-1.6) showed more significant changes than NOE(-3.5). Although both CEST(2.0) and CEST(1.0) increased at the lesion site/cyst, the significance of their peak amplitude changes was not as great as CEST (3.5), compared to respective peak amplitudes of the normal tissues before the spinal cord injury (Fig. 7). Among all the pools, DS(0.0) showed the highest significance for detecting changes at the lesion site/cyst, but only NOE(-1.6) showed a significant decrease for detecting abnormal changes in cDL and rDL regions.

3.7. Group comparison of CEST and NOE measures from AREX$_{mfit}$

The AREX$_{mfit}$ amplitudes from P26sI51 and P51e were highly correlated for NOE$_c$(-3.5), NOE$_c$(-1.6), CEST$_c$(2.0), and CEST$_c$(3.5), while those of DS(0.0) and CEST$_c$(1.0) showed moderate correlations (r at 0.82 and 0.84 respectively) and were more affected by down-sampling (Fig. 8). NOE$_c$(-3.5) and CEST$_c$(3.5) from P26sI51 showed higher correlation (r at 0.97) than other pools with respect to results from P51e. The peak amplitudes at RF offsets farther away from water showed higher correlations between P26sI51 and P51e, indicating that they are less affected by data down-sampling.

Compared to the AREX$_{mfit}$ peak amplitudes of the control at different RF offsets, the respective peak amplitudes from other ROIs showed quite similar trends using both down-sampled data P26sI51 and complete data P51e (Fig. 9). DS$_c$(0.0) still showed high sensitivity for detecting changes at the lesion site and cyst. NOE$_c$(-1.6) changed most in the lesion and cyst, and it also showed significant decreases in cDL. Although both CEST$_c$(2.0) and CEST$_c$(1.0) tended to increase at the lesion site and cyst, significant increases were detected only for CEST$_c$(3.5) compared to normal tissues before injury (Fig. 9).
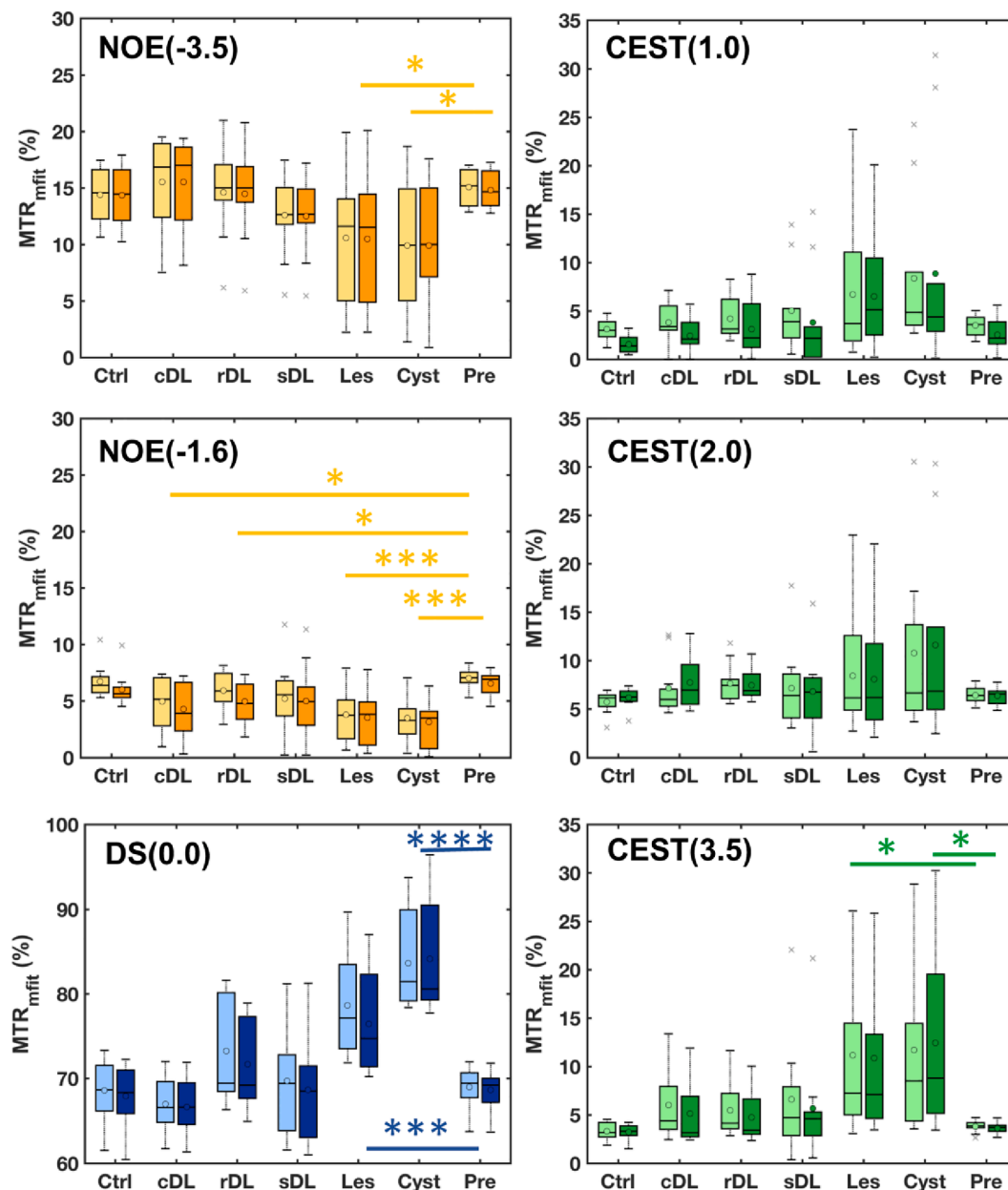
Fig. 7. Comparison of regional percent peak amplitudes of MTR$_{mfit}$ across subjects (N = 10). The results from P51e and P26sI51 are shown in light and dark shades, respectively. Boxplots of regional pool amplitudes of tissues on the control and lesion sides of spinal cords are compared to normal tissues before injury (Pre). The circles and middle lines represent mean and median values respectively. The crosses represent outliers. $*p < 0.02$, $**p < 1 \times 10^{-2}$, $***p < 1 \times 10^{-3}$, and $****p < 1 \times 10^{-5}$ versus the values of normal tissues before injury.

3.8. Sensitivity and specificity of peak amplitudes in detecting cysts

From ROC analyses of MTR$_{mfit}$ measures from P51e (Fig. 10 and Table 1), DS(0.0) showed the largest area under ROC curves (AROC). Both NOE measures were very sensitive to abnormal tissues at the lesion sites, but NOE(-1.6) was more specific than NOE(-3.5). Among all the CEST measures, CEST(3.5) showed highest sensitivity (largest AROC) in detecting cyst. ROC results of MTR$_{mfit}$ peak amplitudes from P26sI51 showed quite similar trends to those from P51e.

From ROC analyses of AREX$_{mfit}$ measures from P51e (Fig. 10 and Table 2), NOE$_c$(-1.6) showed the largest AROC, while DS$_c$(0.0) showed decreased AROC compared to the respective value from MTR$_{mfit}$. Like MTR$_{mfit}$, NOE$_c$(-1.6) from AREX$_{mfit}$ was more sensitive and specific than NOE$_c$(-3.5). Among all the CEST$_c$ measures, CEST$_c$(3.5) again showed highest sensitivity in detecting cyst. ROC results of AREX$_{mfit}$ peak

amplitudes from P26sI51 showed quite similar trends to those from P51e.

4. Discussion

In this study, we characterized multiple proton pools from different molecular origins in different spinal regions after injury and examined the effects of AREX$_{mfit}$ correction on CEST and NOE measurements. Together, we showed that 6-pool fitting from down-sampled data with selected 26 RF offsets provided comparable sensitivity and specificity to 51 RF offsets for detecting regional tissue composition changes following SCI in NHPs. AREX$_{mfit}$ correction improved the accuracy of CEST and NOE estimates.
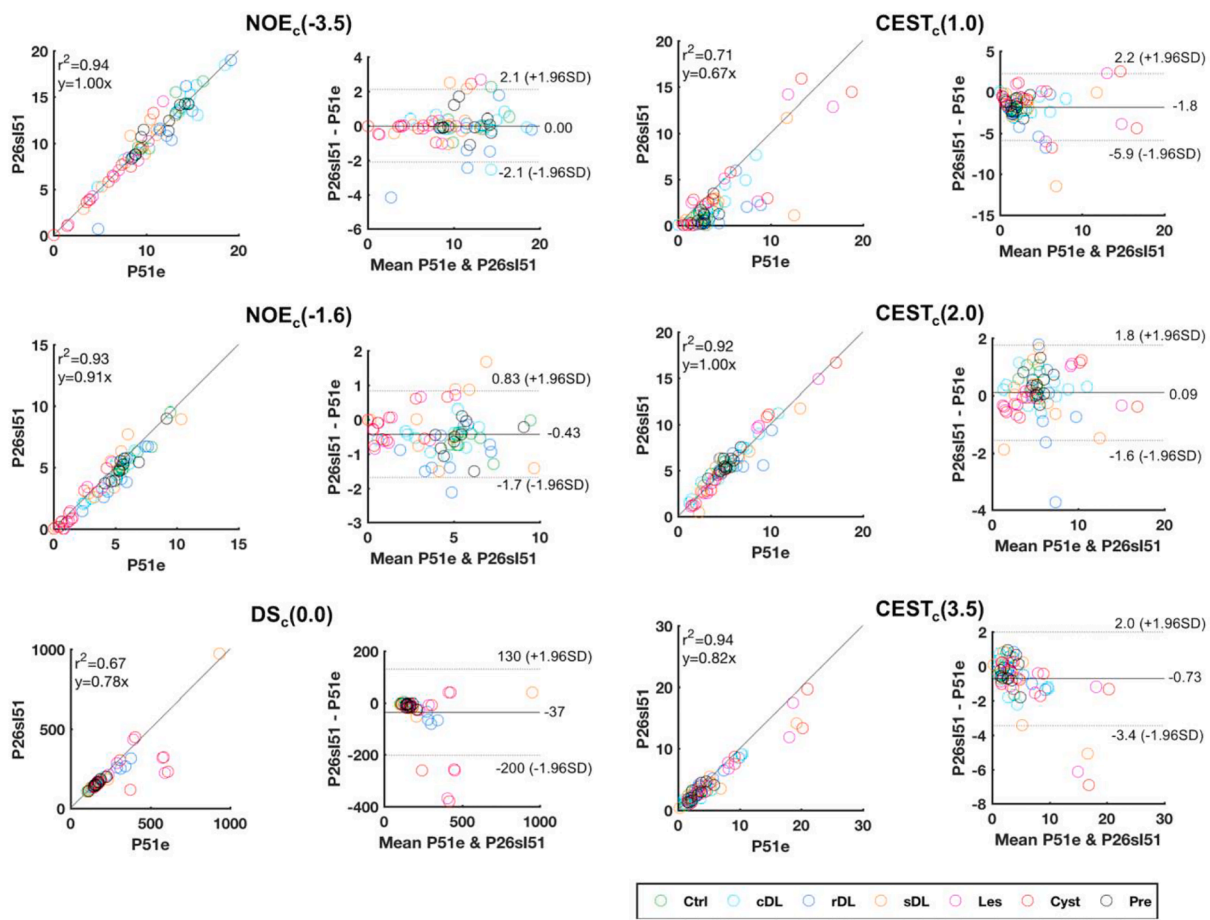
Fig. 8. The comparison of regional AREX$_{mfit}$ measures between P51e and P26sI51. In the Bland-Altman plots, solid line represents the mean difference between measures from the two approaches, whereas the dotted lines are 95% limits of agreement. Results from 7 ROIs of 10 subjects were included for comparison.

4.1. Technique Challenges in CEST and NOE MRI of Spinal Cord at high Field

High signal-to-noise ratio (SNR) and Z-spectra with optimal and sufficient RF offsets are crucial for robust estimates of multiple CEST and NOE measures. Compromises on quality of MRI measures have to be made by considerations of spatial resolution and data acquisition time for each imaging session, even though a customized coil confined to the region of interest can enhance SNR and minimize unwanted signals from moving tissues located farther away (Lu et al., 2020). We recognize that the homogeneities of both B_1 and B_0 fields affect image quality and the spectral characteristics on which CEST and NOE measurements are based (Sup. Fig. S1). Our customized coil provided B_1 coverage for imaging selected spinal cord segments of interest (Lu et al., 2020). The maps show that image quality is generally poorer in tissues close to bone, calcifications and hemorrhagic zones, due likely to the variations in the main field generated by differences in magnetic susceptibility. Our CEST and NOE measurements were taken from relatively homogeneous regions (Sup. Fig. S1 and Fig. 2). In our experience, among all the CEST and NOE measures, CEST(1.0) and NOE(-1.6) are the most sensitive to motion and B_0 variations in *in vivo* studies. The effect of B_0 variations is particularly strong in the early stage after injury when field inhomogeneity could be affected by neck swelling, bleeding, and unstable physiological conditions (Wang et al., 2019).

4.2. Influence of down-sampling on CEST and NOE measures

We found that measures using down-sampled data were capable of detecting regional changes of metabolites surrounding a lesion site with accuracy and precision that are comparable to those using fully-sampled data (Figs. 7 and 9). The results from down-sampled data P26sI51 slightly underestimated multiple pool sizes, especially for those close to water (Figs. 7 and 9). P26sI51 showed lowest levels of bias in the measured values of NOE(-3.5) and NOE$_c$(-3.5) (Figs. 6 and 8). In addition, the P26sI51 data showed reduced correlations with results from fitting for pools closer to water (Figs. 6 and 8) than those farther from water. The potential source of bias for pools close to water peaks using P26sI51 may arise from B_0 and T_2 effects. Overall, we do not expect significant bias using down-sampled data P26sI51.

From optimization studies (Figs. 4-5, Sup. Fig. S4, and Sup. Tables. S2-3), CEST data need to be acquired using selected RF offsets in different ranges based on their respective pool widths. While large intervals can be used for NOE(-1.6) and NOE(-3.5) due to their relatively broad peak widths, shorter intervals need to be considered for DS(0.0), CEST(1.0), and CEST(2.0) and smaller intervals still for CEST(3.5) based on their peak widths (Fig. 1). When appropriate selected down-sampling is applied, the obtained results are as robust as those using densely sampled RF offsets (Figs. 4-5).

Appropriate interpolation could help improve multi-pool fitting using down-sampled data. The interval of the down-sampled data was relatively large, so the application of spline interpolation can help to avoid artificial peaks with unusually high amplitudes and narrow widths, when the range of peak widths is large. In this study, the allowed range for peak width was not tight, and most lower boundaries for peak width were smaller than the interval of down-sampled data (Sup. Table S1). Spline interpolation could improve the fitting stability in this situation, but it should be applied cautiously as a method that could overly smooth the data. Another approach to avoid the above artificial
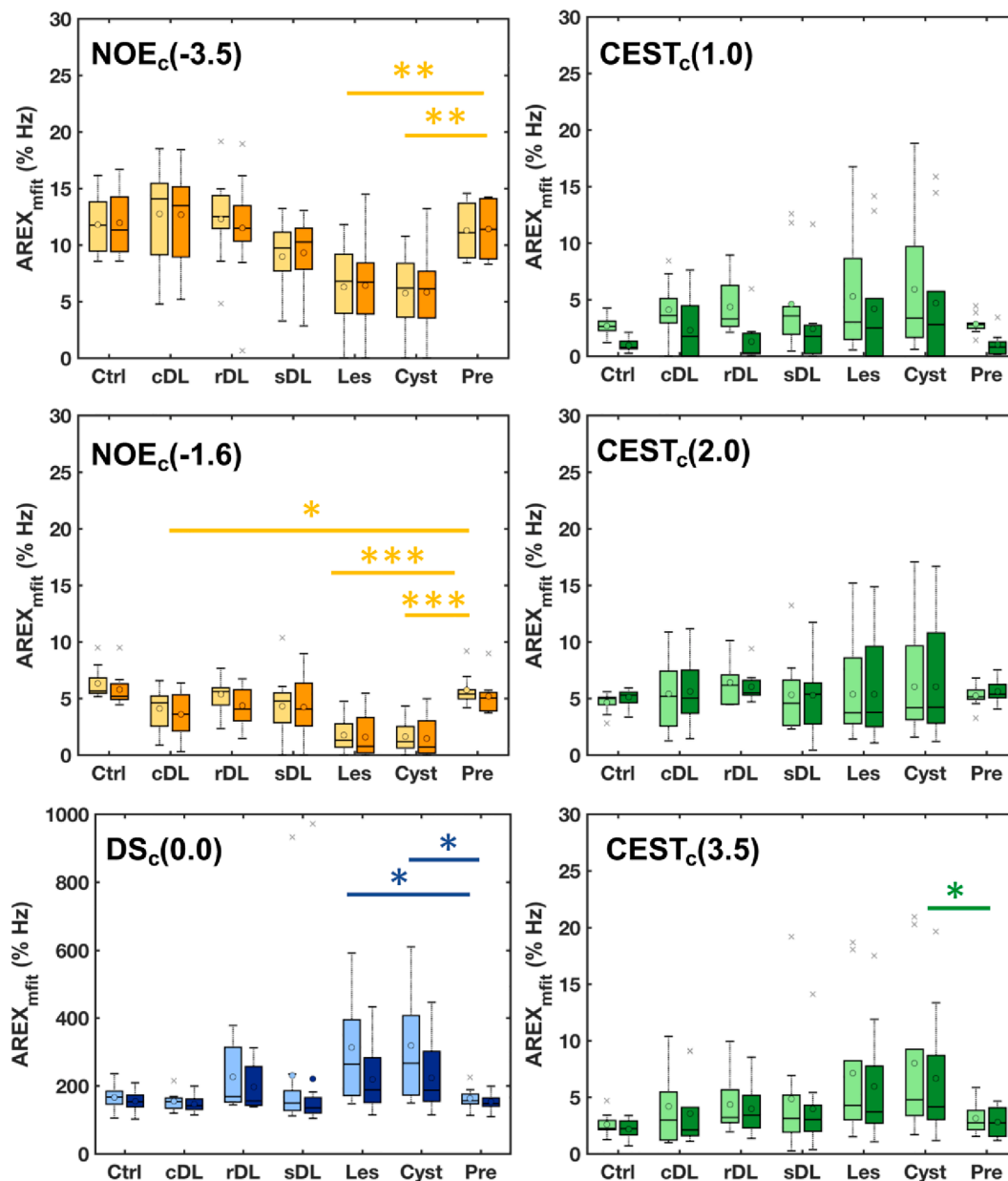
Fig. 9. Comparison of regional percent peak amplitudes of AREX$_{mfit}$ across subjects (N = 10). The results from P51e and P26sI51 are shown in light and dark shades, respectively. Boxplots of regional pool amplitudes of tissues on the control and lesion sides of spinal cords are compared to normal tissues before injury (Pre). The circles and middle lines represent mean and median values respectively. The crosses represent outliers. *$p < 0.05$, **$p < 1 \times 10^{-2}$, ***$p < 1 \times 10^{-3}$ versus the values of normal tissues before lesion.

peaks is to carefully restrict the range of parameters during the fitting, especially the lower boundary of the peak width. The measures from P26sI51 provided comparable sensitivity in assessing lesion-associated damage and recovery (Figs. 6-9) as those from P51e. The potential for bias in the CEST and NOE estimates must be balanced with the reductions in scan time, noise sensitivity, and data analysis time that the down-sampled data acquisition provides. From the above comparisons and considerations, the selected 26 RF offsets are suggested for future data acquisition, which would take about 13 min, for assessing several pools from a multi-pool fitting approach in studying spinal cord injury at 9.4 T.

4.3. The value of regional CEST and NOE measures in monitoring specific spinal pathology and function

For clinical applications, there is a need to shorten the data

acquisition time to minimize physiological influences such as cardiac and respiratory cycles and cerebral spinal fluid (CSF) pulsation. In addition, gross/bulk motion during long data acquisitions may also cause artifacts in the images and bias the estimates of CEST and NOE measures. Advanced fast imaging strategies such as compressed sensing can accelerate CEST data acquisition (Heo et al., 2017). This optimized data acquisition protocol with a low irradiation power (1.0 μT) and using 26 RF offsets (~13 min) can be translated to human spinal cord imaging. It is of note that multiple peaks can be decomposed from the Z-spectrum collected at low irradiation power (0.5–1.5 μT), but they could not be well resolved from fitting due to their severe overlap at higher power (Desmond et al., 2014; Zhang et al., 2017a, 2017b, 2018). Low irradiation power is also preferred in clinical applications due to the restriction of specific absorption rate, the electromagnetic energy absorbed by tissues during MR image acquisition. Noninvasive reliable CEST and NOE measures can provide important information for
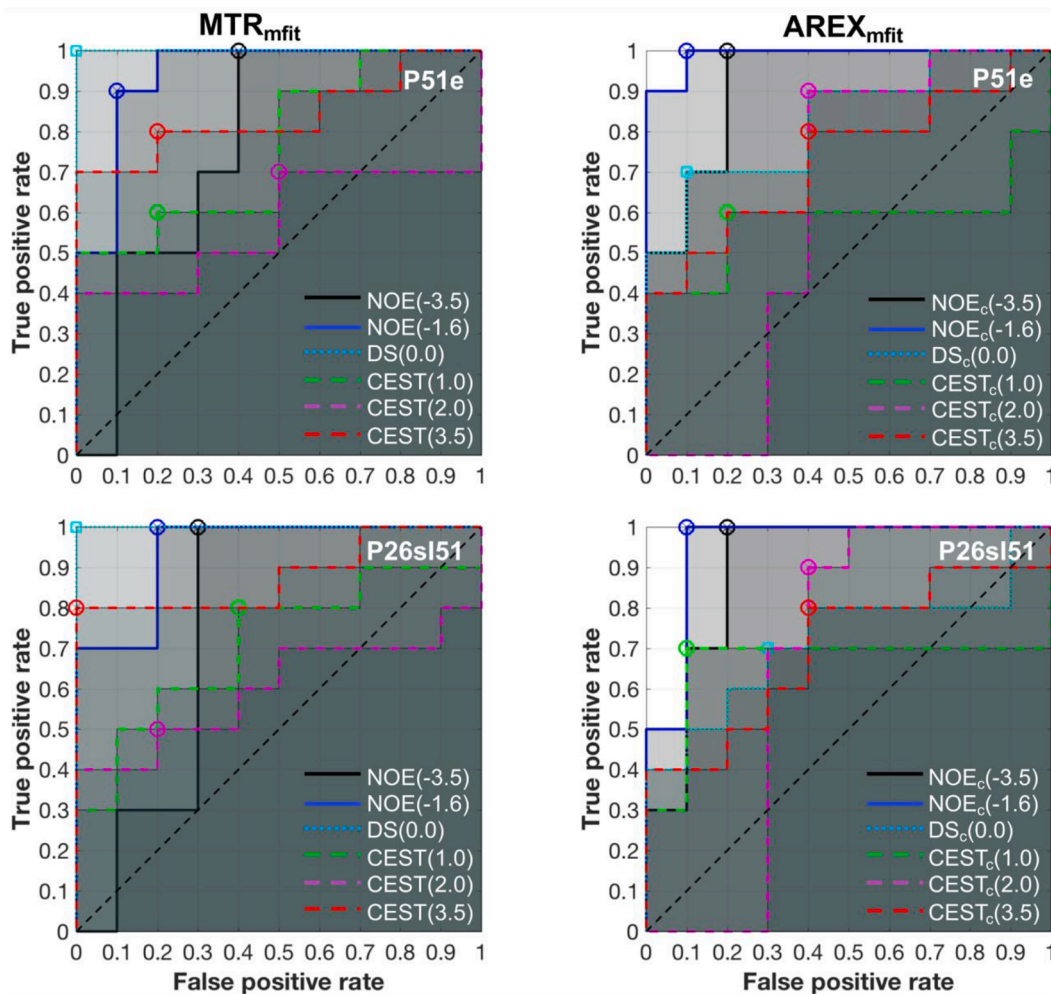
Fig. 10. Sensitivity and specificity of selected MTR$_{mfit}$ and AREX$_{mfit}$ measures in detecting cysts. ROC curves for different measures are indicated in different colors. Areas under ROC curves (AROC) are shaded. Optimum threshold is collocated in the nearest point to (0, 1) in order to maximize the sensitivity (True positive rate) and specificity (1-False positive rate), indicated by circle.

Table 1
ROC results of multi-pool MTR$_{mfit}$ measures of cysts[a]

Pool		Threshold[b]	Sensitivity[b]	Specificity[b]	AROC
P51e	NOE(-3.5)	11.49	1.00	0.60	0.77
	NOE(-1.6)	6.30	0.90	0.90	0.94
	DS(0.0)	75.18	1.00	1.00	1.00
	CEST(1.0)	4.34	0.60	0.80	0.76
	CEST(2.0)	6.30	0.70	0.50	0.57
	CEST(3.5)	4.26	0.80	0.80	0.84
P26sI51	NOE(-3.5)	12.47	1.00	0.70	0.76
	NOE(-1.6)	4.29	1.00	0.80	0.94
	DS(0.0)	74.77	1.00	1.00	1.00
	CEST(1.0)	2.57	0.80	0.60	0.71
	CEST(2.0)	6.86	0.50	0.80	0.60
	CEST(3.5)	4.90	0.80	1.00	0.88

Abbreviation: AROC, area under ROC curve.
[a] Pool amplitudes from MTR$_{mfit}$ (%) from 10 subjects.
[b] Threshold for each parameter shows the optimum value that maximizes the sensitivity and specificity, collocated in the nearest point to (0, 1).

Table 2
ROC results of multi-pool AREX$_{mfit}$ measures of cysts[a]

Pool		Threshold[b]	Sensitivity[b]	Specificity[b]	AROC
P51e	NOE$_c$(-3.5)	8.39	1.00	0.80	0.92
	NOE$_c$(-1.6)	3.86	1.00	0.90	0.99
	DS$_c$(0.0)	190.36	0.70	0.90	0.83
	CEST$_c$(1.0)	2.94	0.60	0.80	0.58
	CEST$_c$(2.0)	4.41	0.90	0.60	0.61
	CEST$_c$(3.5)	3.28	0.80	0.60	0.73
P26sI51	NOE$_c$(-3.5)	7.98	1.00	0.80	0.90
	NOE$_c$(-1.6)	3.40	1.00	0.90	0.95
	DS$_c$(0.0)	161.12	0.70	0.70	0.72
	CEST$_c$(1.0)	1.98	0.70	0.90	0.66
	CEST$_c$(2.0)	4.66	0.90	0.60	0.66
	CEST$_c$(3.5)	3.00	0.80	0.60	0.70

Abbreviation: AROC, area under ROC curve.
[a] Pool amplitudes from AREX$_{mfit}$ (% Hz) from 10 subjects.
[b] Threshold for each parameter shows the optimum value that maximizes the sensitivity and specificity, collocated in the nearest point to (0, 1).

preclinical and clinical studies that aim to track spinal compartment-specific pathology and function over time, and to understand specific behavioral impairments. For example, lateral and dorsal WM tracts carry different types of sensory information (temperature, pain, and discriminative touch) to the brain. Disruptions of these two tracts at high

and middle cervical levels result in various behavioral deficits, including altered temperature and pain sensation and impaired sensorimotor function of hand (e.g., skilled hand use). Damage to the GM in the spinal cord leads to impaired sensory (dorsal horns) and motor behaviors (ventral horns). Here we speculate that the increases in the CEST$_c$(3.5)

peak in the immediate neighboring dorsal GM that appears after the dorsal column lesion could reflect releases of neurotransmitters (made of or synthesized from simple and plentiful precursors such as amino acids) and inflammatory cytokines induced by traumatic injury (Liu et al., 1991; Yezierski, 2000; Oyinbo, 2011). Reduction of NOE_c(-1.6) and $NOE_c(-3.5)$ in GM at the lesion site and in the segments below and above the injury level may indicate the loss of neuronal cell bodies, neuropil and glial cells after injury. It is of note that NOE(-1.6) may reflect membrane lipid components (Zhang et al., 2017a, 2017b) and is sensitive to ischemic stroke without evident structural changes in brain (Zhang et al., 2016). The sources of the CEST and NOE signal changes need to be further validated via tissue microarray neurochemical analysis (Bäckström et al., 2001; Streijger et al., 2017) or possibly ^{1}H MRS, though the latter would be quite challenging given the small volumes involved and issues related to motion and B_0 effects. The reduction of NOE_c(-1.6) in GM caudal to the lesion site may contribute to our previous observations of disrupted functional connectivity between bilateral GM dorsal horns of the spinal segment below injury (Chen et al., 2015). Importantly, these changes in CEST and NOE of dorsal WM and GM on the lesion side significantly correlated with behavioral recovery (Wang et al., 2018b). The changes of CEST and NOE effects from different molecular origins can help us understand how the underlying components contribute to the progression of damage and subsequent recovery of spinal cord tissue, and how the changes of molecular profiles relate to behavioral and functional deficits in each individual with spinal cord injury.

5. Conclusion

These results support the selection of RF offsets and down sampling in CEST imaging of injured spinal cord as a means to reduce total imaging time and/or permit additional signal averaging. $AREX_{mfit}$ can quantify multiple CEST and NOE effects without influence from T_1, DS, and semi-solid MT effects. The current method at high field allows a rapid (~13 mins) and robust approach to characterize the changes in multiple tissue properties caused by injury. The results provide an optimized rapid, sensitive, and accurate protocol for deriving both NOE and CEST effects in spinal cord imaging at high field.

CRediT authorship contribution statement

Feng Wang: Conceptualization, Methodology, Investigation, Data curation, Formal analysis, Writing - original draft. **Zhongliang Zu:** Methodology, Formal analysis, Writing - review & editing. **Tung-Lin Wu:** Data curation, Writing - review & editing. **Xinqiang Yan:** Data curation. **Ming Lu:** Data curation. **Pai-Feng Yang:** Data curation. **Nellie E. Byun:** Project administration, Writing - review & editing. **Jamie L. Reed:** Project administration, Writing - review & editing. **John C. Gore:** Methodology, Writing - review & editing, Funding acquisition, Supervision. **Li Min Chen:** Conceptualization, Writing - review & editing, Funding acquisition, Supervision.

Declaration of Competing Interest

The authors declare that they have no known competing financial interests or personal relationships that could have appeared to influence the work reported in this paper.

Appendix A. Supplementary data

Supplementary data to this article can be found online at https://doi.org/10.1016/j.nicl.2021.102633.

References

Bäckström, T., Sæther, O.D., Norgren, L., Aadahl, P., Myhre, H.O., Ungerstedt, U., 2001. Spinal cord metabolism during thoracic aortic cross-clamping in pigs with special reference to the effect of allopurinol. Eur. J. Vasc. Endovasc. Surg. 22 (5), 410–417.

Chen, L.M., Mishra, A., Yang, P.-F., Wang, F., Gore, J.C., 2015. Injury alters intrinsic functional connectivity within the primate spinal cord. Proc. Natl. Acad. Sci. USA. 112 (19), 5991–5996.

Chen, L.M., Qi, H.-X., Kaas, J.H., 2012. Dynamic reorganization of digit representations in somatosensory cortex of nonhuman primates after spinal cord injury. J. Neurosci. 32 (42), 14649–14663.

Desmond, K.L., Moosvi, F., Stanisz, G.J., 2014. Mapping of amide, amine, and aliphatic peaks in the CEST spectra of murine xenografts at 7 T. Magn. Reson. Med. 71 (5), 1841–1853.

Guest, J.D., Hiester, E.D., Bunge, R.P., 2005. Demyelination and Schwann cell responses adjacent to injury epicenter cavities following chronic human spinal cord injury. Exp. Neurol. 192 (2), 384–393.

Hajian-Tilaki, K., 2013. Receiver operating characteristic (ROC) curve analysis for medical diagnostic test evaluation. Caspian J. Intern. Med. 4 (2), 627–635.

Heo, H.-Y., Zhang, Y.i., Lee, D.-H., Jiang, S., Zhao, X., Zhou, J., 2017. Accelerating chemical exchange saturation transfer (CEST) MRI by combining compressed sensing and sensitivity encoding techniques. Magn. Reson. Med. 77 (2), 779–786.

Kaas, J.H., Qi, H.-X., Burish, M.J., Gharbawie, O.A., Onifer, S.M., Massey, J.M., 2008. Cortical and subcortical plasticity in the brains of humans, primates, and rats after damage to sensory afferents in the dorsal columns of the spinal cord. Exp. Neurol. 209 (2), 407–416.

Kim, M., Gillen, J., Landman, B.A., Zhou, J., van Zijl, P.C.M., 2009. Water saturation shift referencing (WASSR) for chemical exchange saturation transfer (CEST) experiments. Magn. Reson. Med. 61 (6), 1441–1450.

Liu, D., Thangnipon, W., McAdoo, D.J., 1991. Excitatory amino acids rise to toxic levels upon impact injury to the rat spinal cord. Brain Res. 547 (2), 344–348.

Lu, M., Wang, F., Chen, L.M., Gore, J.C., Yan, X., 2020. Optimization of a transmit/receive surface coil for squirrel monkey spinal cord imaging. Magn Reson Imaging 68, 197–202.

Mishra, A., Wang, F., Chen, L.M., Gore, J.C., 2020. Longitudinal changes in DTI parameters of specific spinal white matter tracts correlate with behavior following spinal cord injury in monkeys. Sci. Rep. 10 (1), 17316. https://doi.org/10.1038/s41598-020-74234-2.

Oyinbo, C.A., 2011. Secondary injury mechanisms in traumatic spinal cord injury: a nugget of this multiply cascade. Acta Neurobiol. Exp. (Wars) 71 (2), 281–299.

Qi, H.-X., Chen, L.M., Kaas, J.H., 2011. Reorganization of somatosensory cortical areas 3b and 1 after unilateral section of dorsal columns of the spinal cord in squirrel monkeys. J. Neurosci. 31 (38), 13662–13675.

Qi, H.X., Wang, F., Liao, C.C., Friedman, R.M., Tang, C., Kaas, J.H., Avison, M.J., 2016. Spatiotemporal trajectories of reactivation of somatosensory cortex by direct and secondary pathways after dorsal column lesions in squirrel monkeys. Neuroimage 142, 421–443.

Smith, S.A., Edden, R.A.E., Farrell, J.A.D., Barker, P.B., Van Zijl, P.C.M., 2008. Measurement of T1 and T2 in the cervical spinal cord at 3 tesla. Magn. Reson. Med. 60 (1), 213–219.

Streijger, F., So, K., Manouchehri, N., Tigchelaar, S., Lee, J.H.T., Okon, E.B., Shortt, K., Kim, S.-E., McInnes, K., Cripton, P., Kwon, B.K., 2017. Changes in pressure, hemodynamics, and metabolism within the spinal cord during the first 7 days after injury using a porcine model. J. Neurotrauma 34 (24), 3336–3350.

Stroman, P.W., Wheeler-Kingshott, C., Bacon, M., Schwab, J.M., Bosma, R., Brooks, J., Cadotte, D., Carlstedt, T., Ciccarelli, O., Cohen-Adad, J., Curt, A., Evangelou, N., Fehlings, M.G., Filippi, M., Kelley, B.J., Kollias, S., Mackay, A., Porro, C.A., Smith, S., Strittmatter, S.M., Summers, P., Tracey, I., 2014. The current state-of-the-art of spinal cord imaging: methods. NeuroImage 84, 1070–1081.

Thuret, S., Moon, L.D.F., Gage, F.H., 2006. Therapeutic interventions after spinal cord injury. Nat. Rev. Neurosci 7 (8), 628–643.

Totoiu, M.O., Keirstead, H.S., 2005. Spinal cord injury is accompanied by chronic progressive demyelination. J. Comp. Neurol. 486 (4), 373–383.

Wang, F., Kopylov, D., Zu, Z., Takahashi, K., Wang, S., Quarles, C.C., Gore, J.C., Harris, R.C., Takahashi, T., 2016a. Mapping murine diabetic kidney disease using chemical exchange saturation transfer MRI. Magn. Reson. Med. 76 (5), 1531–1541.

Wang, F., Li, K., Mishra, A., Gochberg, D., Chen, L.M., Gore, J.C., 2016b. Longitudinal assessment of spinal cord injuries in nonhuman primates with quantitative magnetization transfer. Magn. Reson. Med. 75 (4), 1685–1696.

Wang, F., Qi, H.-X., Zu, Z., Mishra, A., Tang, C., Gore, J.C., Chen, L.M., 2015. Multiparametric MRI reveals dynamic changes in molecular signatures of injured spinal cord in monkeys. Magn. Reson. Med. 74 (4), 1125–1137.

Wang, F., Takahashi, K., Li, H., Zu, Z., Li, K.e., Xu, J., Harris, R.C., Takahashi, T., Gore, J. C., 2018a. Assessment of unilateral ureter obstruction with multi-parametric MRI. Magn. Reson. Med 79 (4), 2216–2227.

Wang, F., Wu, T.-L., Li, K.e., Chen, L.M., Gore, J.C., 2019. Spatiotemporal trajectories of quantitative magnetization transfer measurements in injured spinal cord using simplified acquisitions. NeuroImage: Clinical 23, 101921. https://doi.org/10.1016/j.nicl.2019.101921.

Wang, F., Zu, Z., Wu, R., Wu, T.-L, Gore, J.C., Chen, L.M., 2018b. MRI evaluation of regional and longitudinal changes in Z-spectra of injured spinal cord of monkeys. Magn. Reson. Med. 79 (2), 1070–1082.

Wheeler-Kingshott, C.A., Stroman, P.W., Schwab, J.M., Bacon, M., Bosma, R., Brooks, J., Cadotte, D.W., Carlstedt, T., Ciccarelli, O., Cohen-Adad, J., Curt, A., Evangelou, N., Fehlings, M.G., Filippi, M., Kelley, B.J., Kollias, S., Mackay, A., Porro, C.A., Smith, S., Strittmatter, S.M., Summers, P., Thompson, A.J., Tracey, I., 2014. The current state-of-the-art of spinal cord imaging: applications. NeuroImage 84, 1082–1093.

Wu, T.L., Byun, N.E., Wang, F., Mishra, A., Janve, V.A., Chen, L.M., Gore, J.C., 2020. Longitudinal assessment of recovery after spinal cord injury with behavioral measures and diffusion, quantitative magnetization transfer and functional magnetic resonance imaging. NMR Biomed 33 (4), e4216.

Wu, T.-L., Yang, P.-F., Wang, F., Shi, Z., Mishra, A., Wu, R., Chen, L.M., Gore, J.C., 2019. Intrinsic functional architecture of the non-human primate spinal cord derived from fMRI and electrophysiology. Nat. Commun. 10 (1) https://doi.org/10.1038/s41467-019-09485-3.

Yang, P.-F., Wang, F., Chen, L.M., 2015. Differential fMRI activation patterns to noxious heat and tactile stimuli in the primate spinal cord. J. Neurosci. 35 (29), 10493–10502.

Yezierski, R.P., 2000. Pain following spinal cord injury: pathophysiology and central mechanisms. Prog. Brain Res. 129, 429–449.

Zaiss, M., Xu, J., Goerke, S., Khan, I.S., Singer, R.J., Gore, J.C., Gochberg, D.F., Bachert, P., 2014. Inverse Z -spectrum analysis for spillover-, MT-, and T1 -corrected steady-state pulsed CEST-MRI - application to pH-weighted MRI of acute stroke. NMR Biomed. 27 (3), 240–252.

Zhang, X.-Y., Wang, F., Afzal, A., Xu, J., Gore, J.C., Gochberg, D.F., Zu, Z., 2016. A new NOE-mediated MT signal at around −1.6ppm for detecting ischemic stroke in rat brain. Magn. Reson. Imaging 34 (8), 1100–1106.

Zhang, X.Y., Wang, F., Jin, T., Xu, J.Z., Xie, J.P., Gochberg, D.F., Gore, J.C., Zu, Z.L., 2017a. MR imaging of a novel NOE-mediated magnetization transfer with water in rat brain at 9.4T. Magn. Reson. Med. 78 (2), 588–597.

Zhang, X.Y., Wang, F., Li, H., Xu, J.Z., Gochberg, D.F., Gore, J.C., Zu, Z.L., 2017b. Accuracy in the quantification of chemical exchange saturation transfer (CEST) and relayed nuclear Overhauser enhancement (rNOE) saturation transfer effects. NMR Biomed. 30 (7), e3716.

Zhang, X.Y., Wang, F., Xu, J.Z., Gochberg, D.F., Gore, J.C., Zu, Z.L., 2018. Increased CEST specificity for amide and fast-exchanging amine protons using exchange-dependent relaxation rate. NMR Biomed. 31 (2), e3863.